ORIGINAL PAPER

The importance of blood rheology in patient-specific computational fluid dynamics simulation of stenotic carotid arteries

Jessica Benitez Mendieta[1,2] · Davide Fontanarosa[2,3] · Jiaqiu Wang[1,2] · Phani Kumari Paritala[1,2] · Tim McGahan[4] · Thomas Lloyd[5] · Zhiyong Li[1]

Abstract

The initiation and progression of atherosclerosis, which is the main cause of cardiovascular diseases, correlate with local haemodynamic factors such as wall shear stress (WSS). Numerical simulations such as computational fluid dynamics (CFD) based on medical imaging have been employed to analyse blood flow in different arteries with and without luminal stenosis. Patient-specific CFD models, however, have assumptions on blood rheology. The differences in the calculated haemodynamic factors between different rheological models have not been fully evaluated. In this study, carotid magnetic resonance imaging (MRI) was performed on six patients with different degrees of carotid stenosis and two healthy volunteers. Using the 3D reconstructed carotid geometries and the patient-specific boundary conditions, CFD simulations were performed by applying a Newtonian and four non-Newtonian models (Carreau, Cross, Quemada and Power-law). WSS descriptors and pressure gradient were analysed and compared between the models. The differences in the maximum and the average oscillatory shear index between the Newtonian and the non-Newtonian models were lower than 12.7% and 12%, respectively. The differences in pressure gradient were also within 15%. The differences in the mean time-averaged WSS (TAWSS) between the Newtonian and Cross, Carreau and Power-law models were lower than 6%. In contrast, a higher difference (26%) was found in Quemada. For the low TAWSS, the differences from the Newtonian to the non-Newtonian models were much larger, in the range of 0.4–31% for Carreau, 3–22% for Cross, 5–51% for Quemada and 10–41% for Power-law. The study suggests that the assumption of a Newtonian model is reasonable when the overall flow pattern or the mean values of the WSS descriptors are investigated. However, the non-Newtonian model is necessary when the low TAWSS region is the focus, especially for arteries with severe stenosis.

Keywords Atherosclerosis · Newtonian and non-Newtonian models · Carotid bifurcation · Wall shear stress (WSS) · Stenosis · Viscosity models · Phase-contrast magnetic resonance imaging (PC-MRI) · Computational fluid dynamics (CFD)

1 Introduction

Atherosclerosis is a major arterial disease characterized by the thickening and hardening of the vessel walls due to endothelial dysfunction and plaque development. This process results in the deposition of cholesterol and other lipids beneath the intima layer of the artery and the reduction of the cross-sectional area of the lumen, called stenosis. The focal development of atherosclerotic lesions is at regions with complex blood flow patterns such as the carotid bifurcation. Local haemodynamic forces have a profound impact on the initiation and progression of the plaque in the carotid region (Moradicheghamahi et al. 2019). For this reason, the significance of wall shear stress (WSS) has been widely explored and also linked to the progression and rupture

✉ Zhiyong Li
zhiyong.li@qut.edu.au

1 School of Chemistry, Physics and Mechanical Engineering, Queensland University of Technology, Brisbane, QLD 4000, Australia

2 Institute of Health and Biomedical Innovation, Queensland University of Technology, Brisbane, QLD 4000, Australia

3 School of Clinical Sciences, Queensland University of Technology, Brisbane, QLD 4000, Australia

4 Department of Vascular Surgery, Princess Alexandra Hospital, Brisbane, QLD 4102, Australia

5 Department of Radiology, Princess Alexandra Hospital, Brisbane, QLD 4102, Australia

of the carotid plaque which is one of the main factors for ischaemic stroke.

It is well accepted that low WSS is strongly correlated with early stage endothelial dysfunction and identified as an independent marker for initial atherosclerotic changes (Gallo et al. 2018). The combination of low and oscillatory WSS instead was previously correlated with atherosclerotic progression and intimal thickening (Ku et al. 1985). It was also found that in early stages plaque tends to form in areas with low rather than high WSS. However, in the presence of stenosis high WSS was associated with endothelial cell damage and potential denudation (Eshtehardi et al. 2017).

Numerical simulations, employing computational fluid dynamics (CFD) (Long et al. 2000), have then gained increasing interest as a tool to investigate WSS, allowing blood flow analysis in patient-specific geometries and with realistic boundary conditions (Polanczyk et al. 2018; Schirmer and Malek 2012; Dong et al. 2013). The geometry information can be derived from medical imaging modalities, such as magnetic resonance imaging (MRI). Velocity profiles can be extracted from phase-contrast MRI (PC-MRI), as this technique essentially measures the blood flow velocity (Osinnski et al. 1995). The combination of PC-MRI and CFD for haemodynamic analysis generates a powerful tool to understand further details in the blood fluid dynamics on a patient-specific basis. Velocity measurements from PC-MRI have been used previously to compute flow waveforms and to prescribe boundary conditions in carotid artery CFD simulations (Li et al. 2015). Also, recently advanced PC-MRI 3D velocity profiles have been used to prescribe boundary conditions in CFD simulations of the thoracic aorta (Morbiducci et al. 2013; Bozzi et al. 2017; Youssefi et al. 2017, 2018; Pirola et al. 2018). Similarly, there are also some recent studies focusing on the abdominal aorta and reconstruction of blood vessels for computational haemodynamic analysis (Polanczyk et al. 2015, 2016, 2019).

In CFD, it is also possible to implement specific viscosity models for blood flow simulations. Conventionally, experimental and numerical analyses have assumed blood to be a Newtonian fluid, which implies a constant viscosity and therefore a linear relationship between shear stress and shear rate. However, the viscosity of the blood is determined by the plasma viscosity, haematocrit, erythrocyte deformability and aggregability (Robertson and Owens 2009). Studies on blood characterization have shown that especially the aggregation of the erythrocytes into long structures, known as rouleaux, causes the viscosity to increase in areas with a low shear rate (Robertson and Owens 2009; Brust et al. 2013; DiCarlo et al. 2019).

For this reason, multiple studies have suggested that appropriate non-Newtonian models should be adopted as a key factor to produce accurate haemodynamic simulations. From some of these studies, it was observed that Newtonian models underestimate WSS in low-shear stress regions due to the lack of shear-thinning behaviour (Chen and Lu 2004; Huh et al. 2015; Gharahi et al. 2017). Other findings have also shown differences between Newtonian and non-Newtonian models with regard to flattened velocity profiles and larger recirculation zones in non-Newtonian models (Razavi et al. 2011; DiCarlo et al. 2019). In contrast, other studies have shown that in large vessels, the difference between Newtonian and non-Newtonian models is negligible (Ambrosi et al. 2006; Evju et al. 2013; Moradicheghamahi et al. 2019). Previously, the effects of different viscosity models on WSS descriptors were mostly investigated in healthy carotid arteries (Morbiducci et al. 2011; Gharahi et al. 2017). There is still a lack of understanding in the necessity of applying non-Newtonian models to geometries with various degrees of stenosis and considering patient-specific boundary conditions.

Hence, the objective of the present study is to investigate the differences in WSS-based descriptors and pressure gradient, between the Newtonian and non-Newtonian models, in the carotid arteries from patients with different carotid stenosis and healthy volunteers. Eight carotid geometries were divided into four groups ($>70\%$, 50–70%, $<50\%$ stenosis and healthy ones) to analyse the variation in terms of WSS for the different groups. The simulations were performed under pulsatile flow conditions derived from PC-MRI. The velocity contours of the internal carotid artery (ICA) derived from PC-MRI were compared with the CFD simulations for consistency check.

2 Materials and methods

2.1 MR imaging and geometry reconstruction

This study was approved by the Human Research Ethics Committee at the Princess Alexandra Hospital (PAH) in Brisbane, Australia, and Queensland University of Technology's (QUT) Office of Research Ethics and Integrity (HREC/17/QPAH/181). As part of the ethics, informed consent was obtained from all the participants included in this study. Six patients with carotid stenosis (four males and two females, age ranging from 65 to 87 years old) and two healthy volunteers were scanned on a Magnetom Prisma (Siemens Medical Solutions, Malvern, PA, USA) 3T MR whole body system using a 64-channel head/neck coil. Time-of-flight (TOF) magnetic resonance angiograms (MRA) were extracted from the multisequence MRI and imported into an image processing software package, Amira (version 6.0, FEI, at Hillsboro, Oregon, USA). The TOF datasets were composed of 136 contiguous slices with a voxel resolution of 0.52 mm$\times$0.52 mm$\times$1 mm with repetition time (TR) 21 ms and time to echo (TE) 3.1 ms. The region of interest corresponding to the lumen of the carotid

arteries was segmented using a thresholding technique for subsequent 3D reconstruction (Gao et al. 2009, 2011). The degrees of stenosis were calculated according to the North American Symptomatic Carotid Endarterectomy Trial (NASCET) method (Ferguson et al. 1999).

2.2 Blood flow measurement and boundary conditions

Two-dimensional ECG-gated PC-MRI images were acquired at three different locations (common carotid artery (CCA), maximum stenotic region and ICA) for the patients; and two locations (CCA and ICA) for the healthy volunteers at approximately 40 equidistant time frames of the cardiac cycle. The scan parameters were TR/TE = 24.36/3.59 ms, 240×240, coronal field of view 111×111 mm^2 and velocity encoding (VENC) ranging from 60 to 100 cm s^{-1}. By selecting the region corresponding to the lumen of the carotid artery and integrating the axial velocity, the mass flow rate waveform was computed using Segment (version 2.2, Medviso, R6435, Lund, Sweden). The mass flow rate waveform acquired from the CCA was set as the inlet boundary condition. The mass flow rate from the ICA, and in some patients also at the external carotid artery (ECA), was analysed to identify the flow fraction of the ICA and ECA compared to the CCA flow rate. This information was set as a fixed ratio for the outlets. Straight extensions were added to CCA, ICA and ECA, to ensure a fully developed flow and to reduce the influence of the outlet to the carotid bifurcation (Gallo et al. 2014). The geometries were also divided into four groups based on the degree of stenosis and risk level evaluated by radiologists at the Princess Alexandra Hospital (PAH, Woolloongabba, QLD, Australia), as follows: Group 1 (> 70% stenosis including patient one (P1) and patient two (P2)), Group 2 [70–50% stenosis including patient three (P3) and patient four (P4)], Group 3 (< 50% stenosis including patient five (P5) and patient six (P6)) and Group 4 [including healthy one (H1) and healthy two (H2)].

2.3 Computational blood flow modelling

2.3.1 Governing equations and computational models

Blood was modelled as an incompressible fluid with a density of 1050 kg m^{-3}, described by the Navier–Stokes equation for conservation of mass and momentum in three dimensions, as follows:

$$\nabla \cdot v = 0 \tag{1}$$

$$\rho\left(\frac{\partial v}{\partial t} + v \cdot \nabla v\right) = \nabla \cdot \sigma + f \tag{2}$$

where ρ is the (constant) density (kg m^{-3}), v is the velocity vector (m s^{-1}), σ is the stress tensor (Pa), and f is the external body force [Pa], which is assumed to be zero. The finite volume method was employed to solve the governing equations of blood motion and rheology using the software package, ANSYS Fluent (version 19.0, ANSYS, Canonsburg, PA, USA). The fluid domains were divided into approximately 8.5×10^5 cells, using an element size of 0.3 mm, and the CFD simulation was performed using a time step of 0.002 s. A convergence criterion of 0.001 was used for all simulations, and a second-order upwinding method was employed to obtain the solution for each time step. A mesh independence test was also performed to identify the appropriate element size and number of boundary layers for the no-slip boundary condition, applied to the rigid walls.

The models were prescribed with a laminar flow based on the Reynolds number calculated for each geometry. Table 1 shows the Reynolds number at the stenotic region for each patient. The values of Groups 2 and 3 were calculated from the PC-MRI data. For Group 1, the velocity was obtained from CFD due to the limited resolution in the PC-MRI data (as the lumen diameter at stenosis for P1 and P2 was approximately 1.34 mm and 1.77 mm, respectively). The maximum blood velocity acquired from PC-MRI for Groups 2 and 3 (at CCA, ICA and stenosis) and Group 4 (at CCA and ICA) was in the range of 58 to 78 cm s^{-1}, which conformed with the VENC range setting.

2.3.2 Rheological models

In healthy arteries, the shear rate varies from 1 to 1200 s^{-1} over the cardiac cycle, and blood behaves as either Newtonian or non-Newtonian in different phases of the cardiac cycle (Li et al. 2007). The blood viscosity was simulated by applying five different constitutive viscosity models: one Newtonian and four non-Newtonian. For the Newtonian model, the viscosity was set as 0.00345 Pa s. However, shear-dependent viscosity can accurately replicate the nature of blood flow, as blood behaves differently at low flow rates. The most common non-Newtonian models used to capture

Table 1 Calculated Reynolds numbers at the carotid stenotic region of the six patients

Patient number	Reynolds number at systole	Reynolds number at diastole
Patient one (PI)	571	144
Patient two (P2)	1330	157
Patient three (P3)	557	224
Patient four (P4)	835	108
Patient five (P5)	439	94
Patient six (P6)	477	83

blood rheology are the Power-law, Quemada, Cross and Carreau models (Gharahi et al. 2017; Skiadopoulos et al. 2017).

The Power-law is one of the simplest models to represent the non-Newtonian behaviour of fluid, and it is expressed by the following equation:

$$\mu_{min} > \mu = k\dot{\gamma}^{n-1} < \mu_{max} \tag{3}$$

where k is the flow consistency index, $\dot{\gamma}$ is the shear rate or velocity gradient perpendicular to the plane of shear (s^{-1}), and n is the Power-law index, which specifies the extent of the non-Newtonian behaviour (Hussain et al. 1999); μ_{min} and μ_{max} are the minimum and maximum viscosity limits (Pa s).

The Cross model is defined by the following equation:

$$\mu = \mu_\infty + \frac{(\mu_0 - \mu_\infty)}{1 + \left\langle \dot{\gamma}/\gamma_c \right\rangle^n} \tag{4}$$

where μ_o and μ_∞ are the blood viscosities at low and infinite shear rates (Pa s), respectively; γ_c is the reference shear rate (s^{-1}); $\dot{\gamma}$ is the shear rate (s^{-1}); and n is a model constant (Cross 1965).

Quemada formulation is as follows:

$$\mu = \mu_f \left[1 - \frac{1}{2} \frac{K_0 + K_\infty \sqrt{\frac{\|\dot{\gamma}\|}{\gamma_c}}}{1 + \sqrt{\frac{\|\dot{\gamma}\|}{\gamma_c}}} \phi \right]^{-2} \tag{5}$$

where μ_f is the viscosity of plasma (Pa s), ϕ is the haematocrit, k_o is maximum volume fraction for zero shear rate, k_∞ is the maximum volume fraction for infinite shear rate, $\dot{\gamma}$ is the shear rate (s^{-1}) and γ_c is the characteristic rate of rouleaux formation/degradation (s^{-1}) (Quemada 1978).

Carreau model is similar to Power-law, as it is a generalization of a Newtonian model, and it is described by the following equation:

$$\mu = \mu_\infty + (\mu_0 - \mu_\infty)[1 + (\lambda\dot{\gamma})^2]^{(n-1)/2} \tag{6}$$

where μ_o is the viscosity at zero shear rate (Pa s), μ_∞ is the viscosity at infinite shear rate (Pa s), λ is the relaxation time (s), $\dot{\gamma}$ is the shear rate (s^{-1}) and n is the power index (Cho and Kensey 1991). The parameters used for each viscosity model are summarized in Table 2.

One of the main characteristics for each model is from which shear rate they calculate a constant viscosity. In the case of the Carreau model, it is reached for $\dot{\gamma} > 10^4 \ s^{-1}$, whereas Cross matches the constant viscosity approximately at shear rates $\dot{\gamma} > 10^2 \ s^{-1}$ and Power-law approximately at $\dot{\gamma} > 10^3 \ s^{-1}$. Quemada shows a semi-constant behaviour at $\dot{\gamma} > 10^2 \ s^{-1}$, as shown in Fig. 1. The viscosity models were adjusted to a haematocrit (Ht) of 0.45 which corresponds to a typical normal value in males and females. In the Newtonian

Table 2 Parameters used for the viscosity models

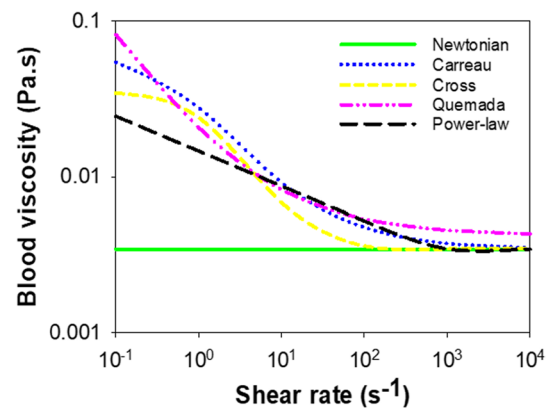| Model	Parameters
Newtonian	$\mu_\infty = 0.00345$ Pa s
Power-law	$k = 0.01467$
	$n = 0.7755$
	$\mu min = 0.00345$
	$\mu max = 0.025$
Cross	$\mu_o = 0.0364$ Pa s
	$\gamma_c = 2.63 \ s^{-1}$
	$n = 1.45$
Quemada	$\phi = 0.45$ for haematocrit
	$\mu_f = 0.0012$ Pa s
	$\gamma_c = 1.88 \ s^{-1}$
	$k_o = 2.07$
	$k_\infty = 4.33$
Carreau	$\mu_o = 0.056$ Pa s
	$\lambda = 3.131$ s
	$n = 0.3568$

Fig. 1 Relations between shear rate and viscosity for the different viscosity models

model, a Ht of 0.45 corresponds to a constant viscosity of 0.00345 Pa s (Mehri et al. 2018) and in the non-Newtonian models to the viscosity at high shear rates, excepting Quemada which is maintained above 0.00345 Pa s. User-defined functions (UDF) were developed for discretization of Cross and Quemada; for Carreau and Power-law, the viscosity models available in Fluent (version 19.0) were employed.

2.3.3 WSS-based haemodynamic descriptors

WSS-based descriptors were investigated using them as endpoints, including the time average WSS (TAWSS), oscillatory shear index (OSI) and the relative residence time (RRT) (Soulis et al. 2011) which indicates the time of residence that particles spend at the endothelium. Previous studies have

recommended RRT as a robust metric for low and oscillating shear (Lee et al. 2009). These descriptors were computed as follows:

$$TAWSS = \frac{1}{T} \int_0^T |\tau_w| dt \tag{7}$$

$$OSI = \frac{1}{2} \left[1 - \frac{\left| \int_0^T \tau_w dt \right|}{\int_0^T |\tau_w| dt} \right] \tag{8}$$

$$RRT = \frac{1}{(1 - 2 \times OSI) \times TAWSS} \tag{9}$$

where T is the entire cardiac cycle duration, and τ_w is the shear stress at the artery wall. For TAWSS, the analysis was performed using the whole geometry as well as a specific region of interest (ROI) at the bifurcation or the stenotic region. In order to understand more about the small difference between the maximum and average TAWSS values from Carreau, Cross, Power-law and Newtonian models, the viscosity range calculated using these models was examined.

2.3.4 Pressure gradient analysis

In some instances, high blood pressure has been correlated with cerebral strokes and directly linked to arterial thickening. It was also claimed that high blood pressure might lead to the initiation of atherosclerosis (Augst et al. 2007). Therefore, apart from WSS descriptors, contours of the pressure gradient acting on the arterial wall were also investigated.

2.4 Velocity comparison between CFD models and PC-MRI

PC-MRI images were registered to TOF to identify the spatial location of the planes at ICA within the luminal geometry. The comparison was carried out at the ICA at the peak systolic phase because at this specific point the flow is in the axial direction at all locations within the lumen. The velocity contours corresponding to the identified location from CFD were compared to the PC-MRI velocity contour, and the difference between them was analysed.

3 Results

3.1 Flow rate profile, outlet ratios and geometries

The final reconstructed geometries are shown in Fig. 2. Figure 2 also illustrates the ICA/ECA outflow ratios set for the outlets for each geometry. The CCA flow rate profiles, acquired from PC-MRI, were used as inlet flow boundary

conditions. The reconstructed geometries demonstrated that atherosclerotic plaques often occurred in the ICA. The calculated degree of stenosis for each patient was as follows: P1 75%, P2 72%, P3 58%, P4 66%, P5 22% and P6 15%.

3.2 WSS descriptors

3.2.1 TAWSS

Figure 3 shows the comparison in terms of the spatially averaged TAWSS for the eight geometries, in the complete geometry (Fig. 3) and in the selected ROI in the stenotic region (Fig. 3). For both the whole geometry and the ROI, there was no remarkable difference in TAWSS between Newtonian, Carreau, Cross and Power-law models. However, higher TAWSS values were found in the Quemada model, and the differences increased with the degree of stenosis. For the complete geometry, TAWSS started from approximately 2.5 Pa for the healthy geometries to 10 Pa for the geometries with the highest stenosis. The percentage differences in TAWSS for the non-Newtonian models comparing to the Newtonian model (as a reference) for all the geometries are summarized in Table 3. The highest percentages were provided by Quemada, followed by Carreau which presented a maximum of 6%. Cross and Power-law predicted the lowest percentages with a maximum of 3.2%.

When focusing on the ROI, the differences between models in Groups 3 and 4 (P5, P6, H1, H2) become smaller. In the ROI, the TAWSS was around 1.8 Pa for the healthy geometries and approximately 28 Pa for the highest stenosis case. Comparing the average TAWSS values between the complete geometry and the ROI, there was an approximately threefold increment in P1, P2 and P4 and twofold in P3. On the contrary, the TAWSS values were lower in the ROI than those in the complete geometries in Groups 3 and 4 (P5, P6, H1, H2).

The total maximum WSS values presented a similar behaviour to the average values between the models. Carreau, Cross and Power-law predicted similar values with the highest percentage difference at 0.7%. Quemada also predicted the highest TAWSS values, and the percentage difference for each patient compared to the Newtonian model varied from 13 to 17%. Visual inspection of the TAWSS contours also showed no remarkable differences between the models.

The TAWSS distributions of four geometries (P1, P3, P5 and H1) at the end of the cardiac cycle, as an example from each group, are depicted in Fig. 4. A maximum value of 1 Pa was used to better show the low WSS regions, as reported in previous studies (Malek and Alper 1999; LaDisa et al. 2005). It can be observed that, regardless of the assumed viscosity model, the disturbances were captured in the same sites. However, Quemada simulations showed the smallest region
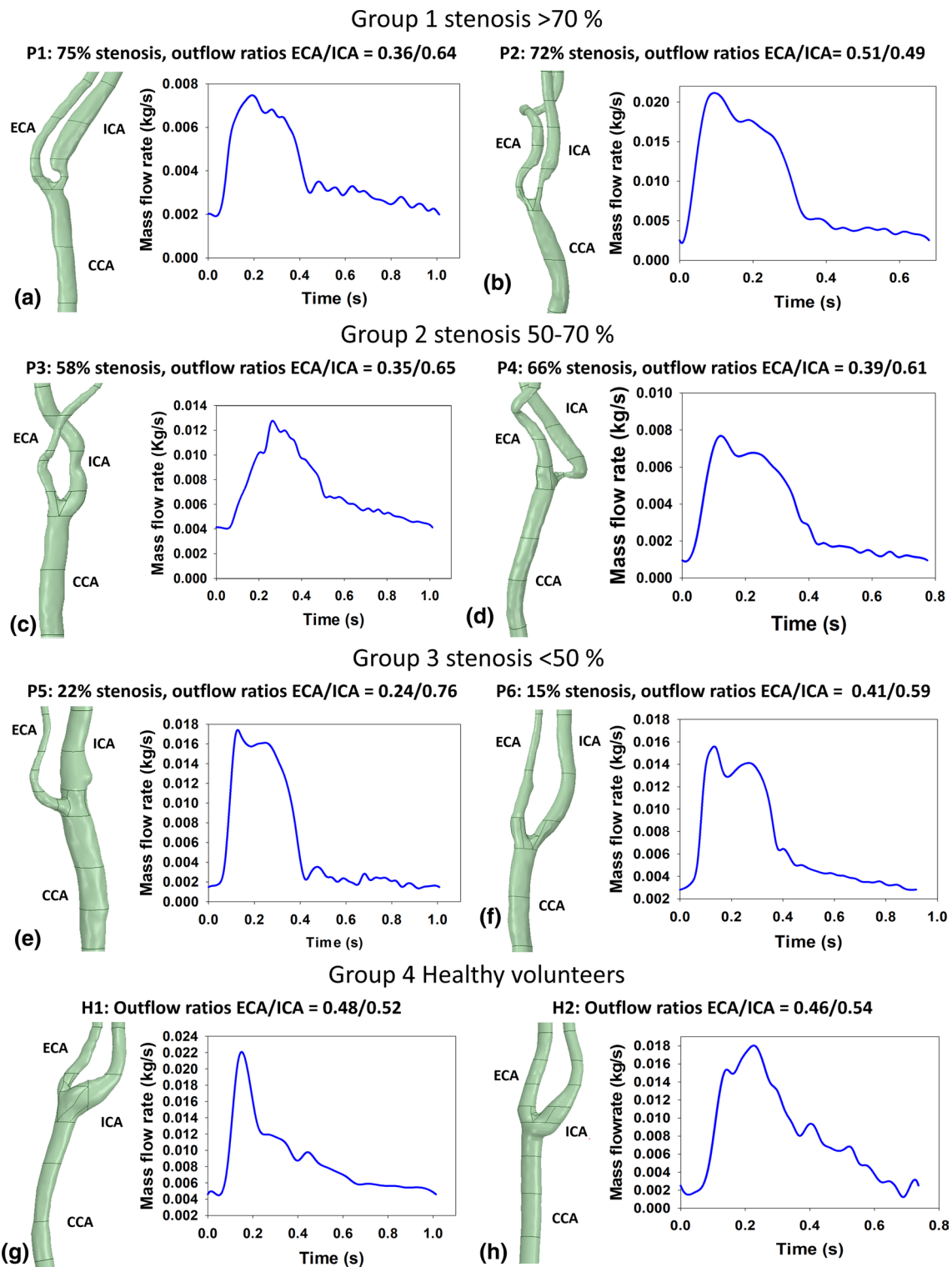
Fig. 2 3D reconstructed carotid artery geometries (left) and the interpolated mass flow rate waveform for one cardiac cycle set as inlet boundary condition at the CCA (right). The outflow ratio was set as outlet boundary conditions at ICA and ECA. Group 1 includes **a** patient one (P1), **b** patient two (P2), Group 2 includes **c** patient three (P3), **d** patient four (P4), Group 3 includes **e** patient five (P5), **f** patient six (P6), and Group 4 includes **g** healthy volunteer one (H1) and **h** healthy volunteer two (H2)

Fig. 3 The mean TAWSS for the eight cases calculated from the six viscosity models for **a** complete geometry and **c** ROI at the stenosis region, **b** a TAWSS contour example of a complete geometry and **d** a TAWSS contour example of ROI at the stenotic region
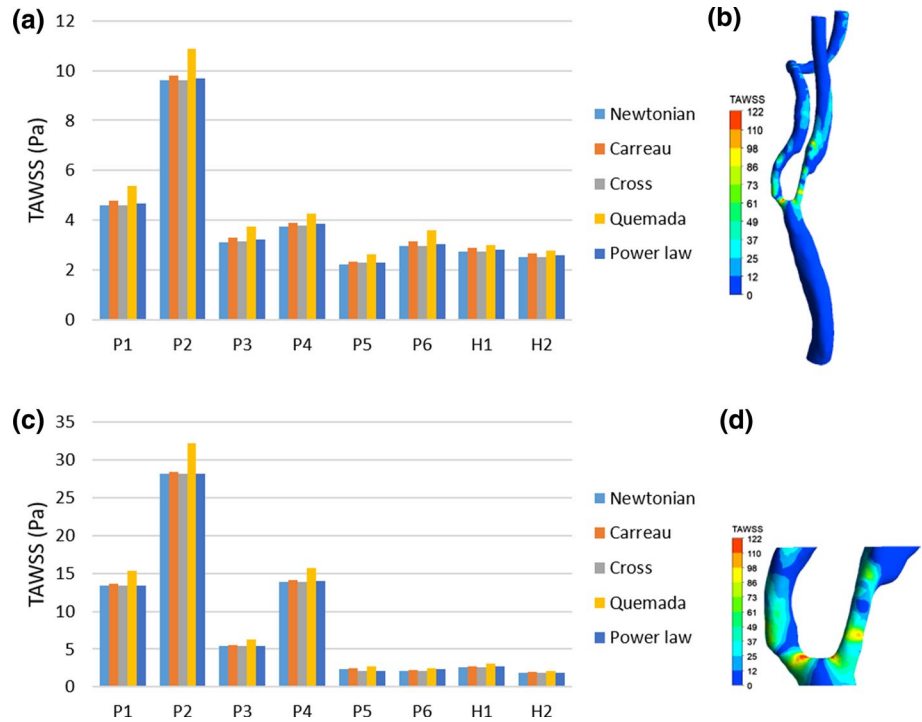

Table 3 Percentage differences in mean TAWSS between the non-Newtonian models and the Newtonian model (as a reference)

	Patient	Carreau (%)	Cross (%)	Quemada (%)	Power-law (%)
Group 1	P1	4	0.17	15	1.8
	P2	1.86	0.02	26	0.08
Group 2	P3	5.5	0.3	18	3.1
	P4	3.35	0.32	13	2.5
Group 3	P5	5	3	16	3
	P6	6.1	0.3	20	3.2
Group 4	H1	6.4	0.3	9.3	3
	H2	6	0.3	10	2.8

at low TAWSS for all geometries. The lowest levels of WSS had the strongest appearance in the Newtonian and Cross models, where the effect of not having the shear-thinning assumption and allowing a non-constant viscosity above $\dot{\gamma} < 100$ can be seen on the TAWSS. Carreau and Power-law predicted intermediate values among the viscosity models. The minimum TAWSS values compared to the maximum and average values had a larger variation between models; however, the closest values were seen in both healthy cases. On the contrary, for both geometries in Group 1, the percentage differences were prominent comparing the Newtonian to the non-Newtonian models, excepting Cross. In P1, the percentage differences in minimum TAWSS were 31% for Carreau, 5% for Cross, 51% for Quemada and 41% for Power-law. Similarly, for P2 the percentage differences were

30% for Carreau, 9% for Cross, 38% for Quemada and 37% for Power-law. For visualization purposes, Fig. 5 shows the difference in TAWSS contours between Newtonian and non-Newtonian models of P1. The maximum difference was seen for the Quemada model at the stenosis region, followed by Carreau. The location of the maximum difference for Cross and Power-law was at the ICA with a difference of 0.12 and 1.04 Pa, respectively.

3.2.2 Viscosity range analysis

In order to understand the difference between the Newtonian model and the non-Newtonian models in depth (Carreau, Cross, Power-law), viscosity values were evaluated across the entire geometry of P1. For Carreau, it was found that the viscosity ranges from 0.00352 Pa s to 0.023 Pa s. On closer inspection, it was identified that the viscosity values in the range of 0.00345–0.00431 Pa s (which matches the maximum viscosity at high shear rates in human blood (DiCarlo et al. 2019)) accounted for 50% for Carreau, 98% for Cross and 57% for Power-law. For this specific geometry with > 70% stenosis, the range of the shear rate was approximately 2.7 s^{-1} to 10,800 s^{-1}. Similarly, 96% of the data was concentrated in the range of 2.7 s^{-1} to 1000 s^{-1}, with an average value of 342 s^{-1}.

3.2.3 OSI

Figure 6 shows the OSI contours for four cases, in the range of 0–0.5. A low OSI corresponds to a minimum or
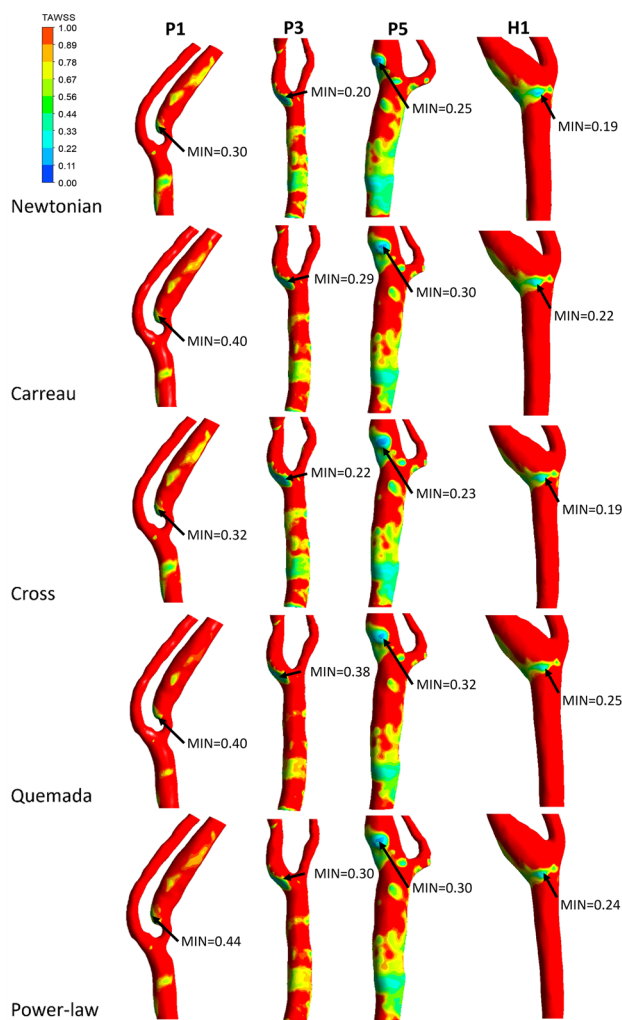
Fig. 4 TAWSS contour plots over one cardiac cycle for the different viscosity models for four cases (P1 from Group 1, P3 from Group 2, P5 from Group 3 and H1 from Group 4). The locations of the minimum TAWSS are shown in arrows. The geometries were oriented to show the region of interest

no changes of WSS vectors with respect to the main direction of flow, whereas a high OSI corresponds to deviations of WSS vectors from the main flow in multiple directions through the cardiac cycle. The maximum OSI occurred at either the ICA or the bifurcation. For Groups 3 and 4, the oscillation was concentrated at the bifurcation; however, in Groups 1 and 2, it was at the ICA after stenosis. The different viscosity models captured similar locations for the main disturbances across the geometries. However, Quemada produced a stronger and larger area of oscillation. Interestingly, the comparison in terms of the maximum values of OSI for all the geometries and viscosity models showed that the maximum difference was only 12.7%, between the Newtonian and non-Newtonian models. Even though the difference was small, the Newtonian and Cross

models presented the lowest oscillation. For the average OSI value, the maximum percentage difference was also approximately 12%.

3.2.4 RRT

Figure 7 presents the RRT contours in P1 as an example. The results showed that concave and post-stenotic regions of the carotid artery were prone to high RRT values, and a similar pattern was depicted between the different viscosity models. The Newtonian and Cross models were more susceptible to provide higher RRT values in almost all geometries.

3.3 Pressure gradient

Contour plots of the pressure gradient for all the geometries are presented in Fig. 8. The results were from the Newtonian models to avoid redundancy as the values and the locations for the highest pressure values were almost identical for all the assumed viscosity models. The highest pressure in the healthy cases and P6 (with a low degree of stenosis) was at the apex. In P1, P2 and P4, the highest pressure was at the stenotic region. For P3 and P5, the highest pressure was at the ECA due to the complexity of the luminal geometry. Similar to the pattern observed for TAWSS, the pressure progressively increased with the degree of stenosis by approximately ten times. Comparing the viscosity models, Quemada provided higher average pressure values compared to the other models, as shown in Fig. 8. The highest pressure locations correlated to the locations where the highest TAWSS values were observed for all cases. The highest percentage difference in maximum pressure was 15% between the Newtonian model and the non-Newtonian models. Even for the severe stenosis cases, the pressure difference between models was not substantial.

3.3.1 CFD and PC-MRI comparison

Figure 9 shows a qualitative comparison between the PC-MRI and the CFD results in terms of axial velocity at systole in a cross section at the ICA. The CFD results were from simulations obtained by applying a Newtonian model. In most cases, CFD tended to overestimate the maximum velocity values even though the overall flow rate and the general flow pattern were similar. The highest percentage difference in the axial velocity between PC-MRI and CFD was 61% for the geometries with the highest stenosis (P1 and P2). On the contrary, in P4 it was seen that the maximum axial velocity was the same. For the rest of the geometries, the percentage difference ranged from 15 to 55%.
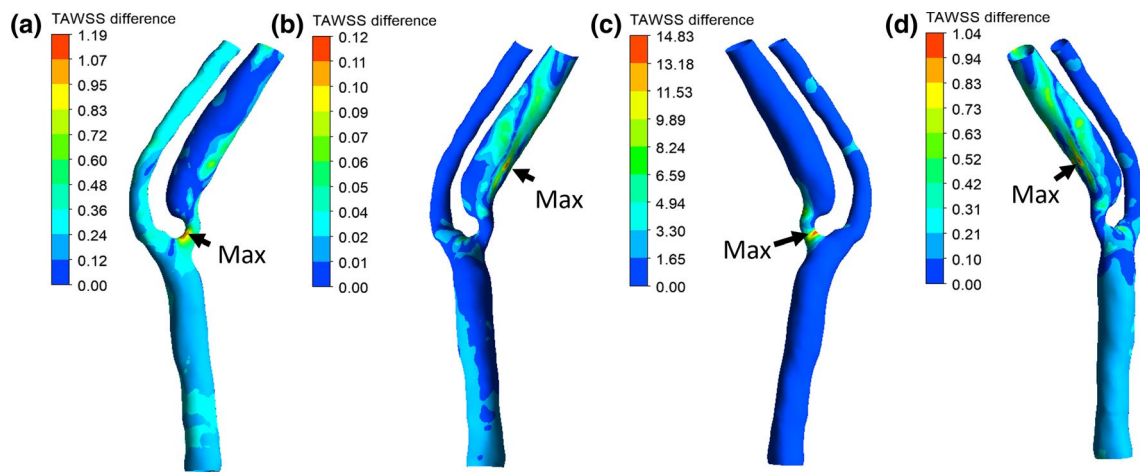
Fig. 5 TAWSS difference for P1 between the Newtonian model and **a** Carreau, **b** Cross, **c** Quemada and **d** Power-law. The geometry was rotated to show the location for the maximum difference between models, indicated by arrows
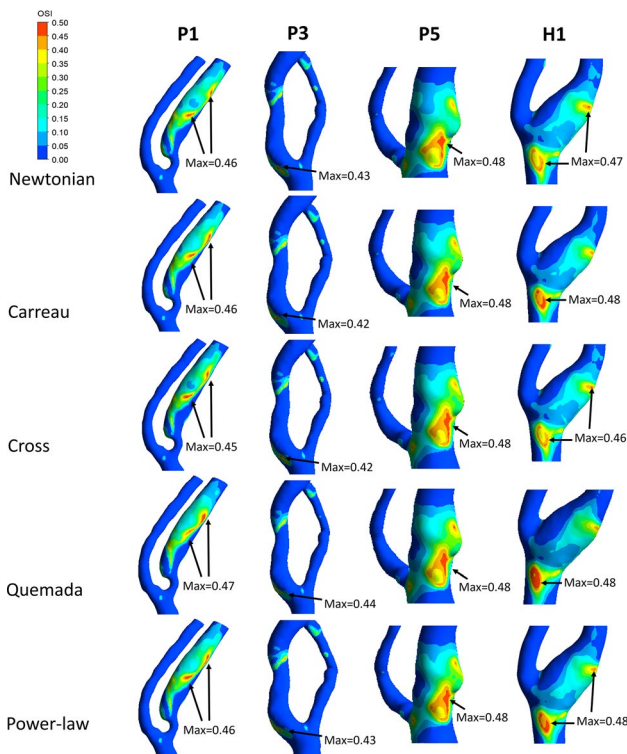

Fig. 6 OSI contour plots for the different viscosity models for four cases. The geometries were oriented to show the region of interest

4 Discussion

Realistic, accurate and less computationally expensive CFD simulations are essential in understanding the initiation and progression of atherosclerosis, as well as in predicting the evolution of cardiovascular diseases. WSS is an important metric that has been linked to different stages of atherosclerosis progression. For this reason, eight carotid arteries: six from patients with different degrees of stenosis and two healthy volunteers, were recruited for haemodynamic analysis by applying five different viscosity models. The main aim was to evaluate the difference in WSS-based parameters between the Newtonian and the non-Newtonian models. The subjects were divided into four groups according to the degree of stenosis, and the calculated WSS descriptors were compared between viscosity models. To our knowledge, this is the first study to investigate the effects of non-Newtonian viscosity models using geometries with increasing levels of stenosis from patient MRI data and patient-specific boundary conditions.

Five viscosity models were employed for simulations which were adjusted to a Ht value of 0.45. The Newtonian model uses a constant viscosity of 0.00345 Pa s, which also represents the viscosity at high shear rates for the non-Newtonian models, e.g. Cross, Carreau and Power-law. Even though the Quemada model was also adjusted to Ht = 0.45, the calculate viscosity at high shear rates was 0.00431 Pa s. This increment resulted in higher WSS values than those of the other viscosity models, which suggests that the proficiency of this model is limited to low shear rates.

In relation to WSS descriptors, the assumption of a Newtonian model in image-based simulations for different degrees of stenosis with patient-specific boundary conditions is reasonable for OSI. This is supported by the percentage difference at maximum and average values comparing Newtonian and non-Newtonian values, as for both measurements the highest percentage was approximately 12%. Figure 6 also shows the negligible differences between OSI profiles acquired by applying the different rheology models.

Fig. 7 RRT contour plots for P1 for the different viscosity models as follows: **a** Newtonian, **b** Carreau, **c** Cross, **d** Quemada and **e** Power-law
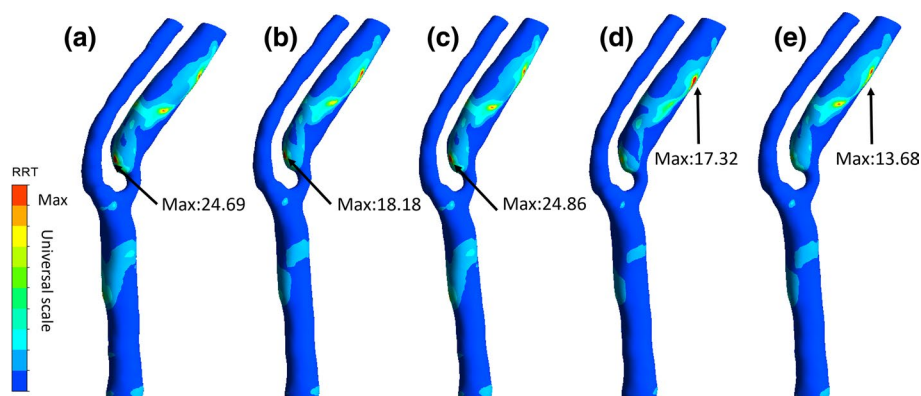
For TAWSS, the analysis of the maximum and average values resulted in a low percentage difference comparing to Newtonian, with a maximum percentage of 6% for Carreau, Cross and Power-law and, however, a 26% for Quemada. The similarity with respect to TAWSS (maximum and average) and OSI values calculated by the Newtonian and non-Newtonian models (Carreau, Cross and Power-law) can be attributed to the fact that average shear rates for all the geometries were in the range of 115–402 s^{-1}, an area with no prominent changes in viscosity according to Fig. 1.

However, when analysing the low TAWSS values, the percentage differences between Newtonian and Carreau, Cross, Quemada and Power-law ranged at 0.4–31%, 3–22%, 5–51% and 10–41%, respectively. This result is due to the shear-thinning behaviour prescribed by these viscosity models which calculates higher WSS values at low shear rates, compared to the Newtonian model which calculates lower values resulting in a possible overestimation of the low TAWSS region. These findings suggest Non-Newtonian models should be employed to investigate the regions prone to low WSS and hence to the evaluation of atherosclerotic initiation regions, especially for carotid arteries with stenosis > 50%. However, it is important to mention that non-Newtonian properties of blood are exhibited at shear rates lower than 100 s^{-1} (Berger and Jou 2000). Cross is the viscosity model that better fits the rheological behaviour of blood, thus resulting in a smaller difference in TAWSS range from the Newtonian model. The analysis of the number of nodes that laid in the viscosity range between 0.00345 and 0.00431 Pa s for the Cross model explains the close proximity of the results with the Newtonian model. On the other hand, the shear rate range analysis also demonstrated that in stenotic vessels the shear rate can reach values larger than 10,000 s^{-1}. The finding of a relatively small impact of the viscosity models to TAWSS and OSI in the carotid bifurcation is consistent with previous studies (Lee and Steinman 2007; Morbiducci et al. 2011; Gharahi et al. 2017). The results also agree with the study performed by Yang et al. (2007), where the comparison between Newtonian and

non-Newtonian models was analysed using fluid–structure interaction (FSI) simulations.

RRT was firstly explored in this paper in realistic carotid geometries with various degrees of stenosis. Although the maximum values differ among the viscosity models, RRT prescribed the same location where particles spent the longest time. From visual inspection of the RRT profiles, there were no major discrepancies between models, as shown in Fig. 7. This result is consistent with previous studies (Lee et al. 2009; Morbiducci et al. 2010) which stated that RRT captures the main features of TAWSS (specifically low WSS) and OSI. Additionally, the results show that the differences in pressure gradient, in terms of location, maximum and average values, were negligible, between the viscosity models, except for Quemada.

The computational simulation results were also compared with PC-MRI measurements. The axial velocity profile from a cross section at the ICA was used for the comparison. In general, a similar flow pattern was found between the CFD results and the measurements; however, CFD tends to overestimate the maximum velocity compared to PC-MRI, and previous studies (Steinman et al. 2002; Gharahi et al. 2017) have also shown a similar finding. One of the main reasons for the difference may be that we have neglected the movement of the arterial walls in the CFD study by assuming rigid walls in calculating the exact flow rate ratios between the ICA and ECA.

5 Study limitations

The main limitation of this study is the assumption of rigid walls; however, the purpose of this study was to compare the CFD results between different viscous models and the same conditions were used between the models. Another limitation is that just two geometries were included in each group which is not sufficient for performing a compelling statistical analysis. However, this proof-of-concept study has provided direct and quantitative case-by-case comparisons with regard

Fig. 8 **a** Pressure gradient contour plots for the eight cases and **b** comparison of the average pressure gradient between different models
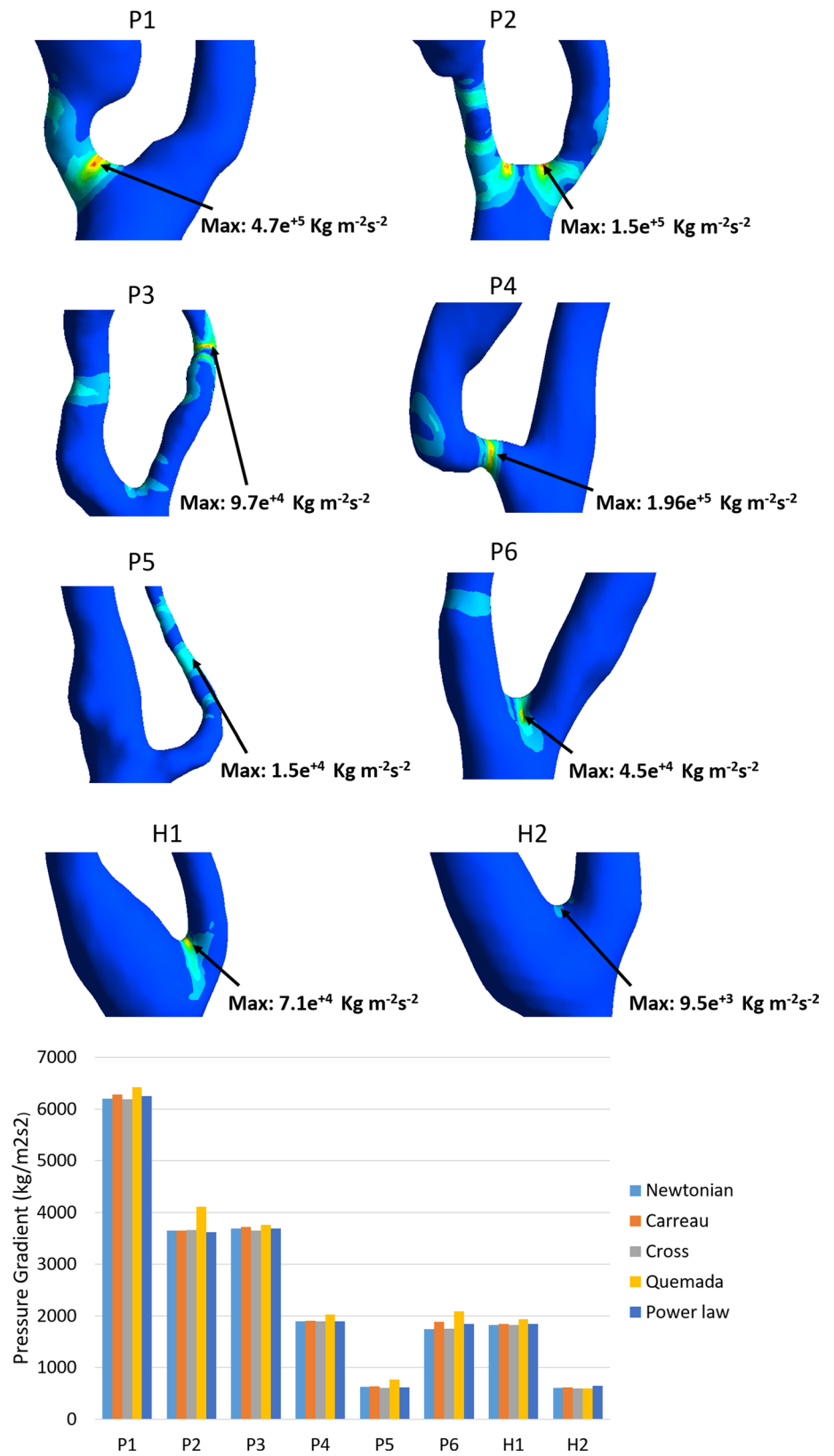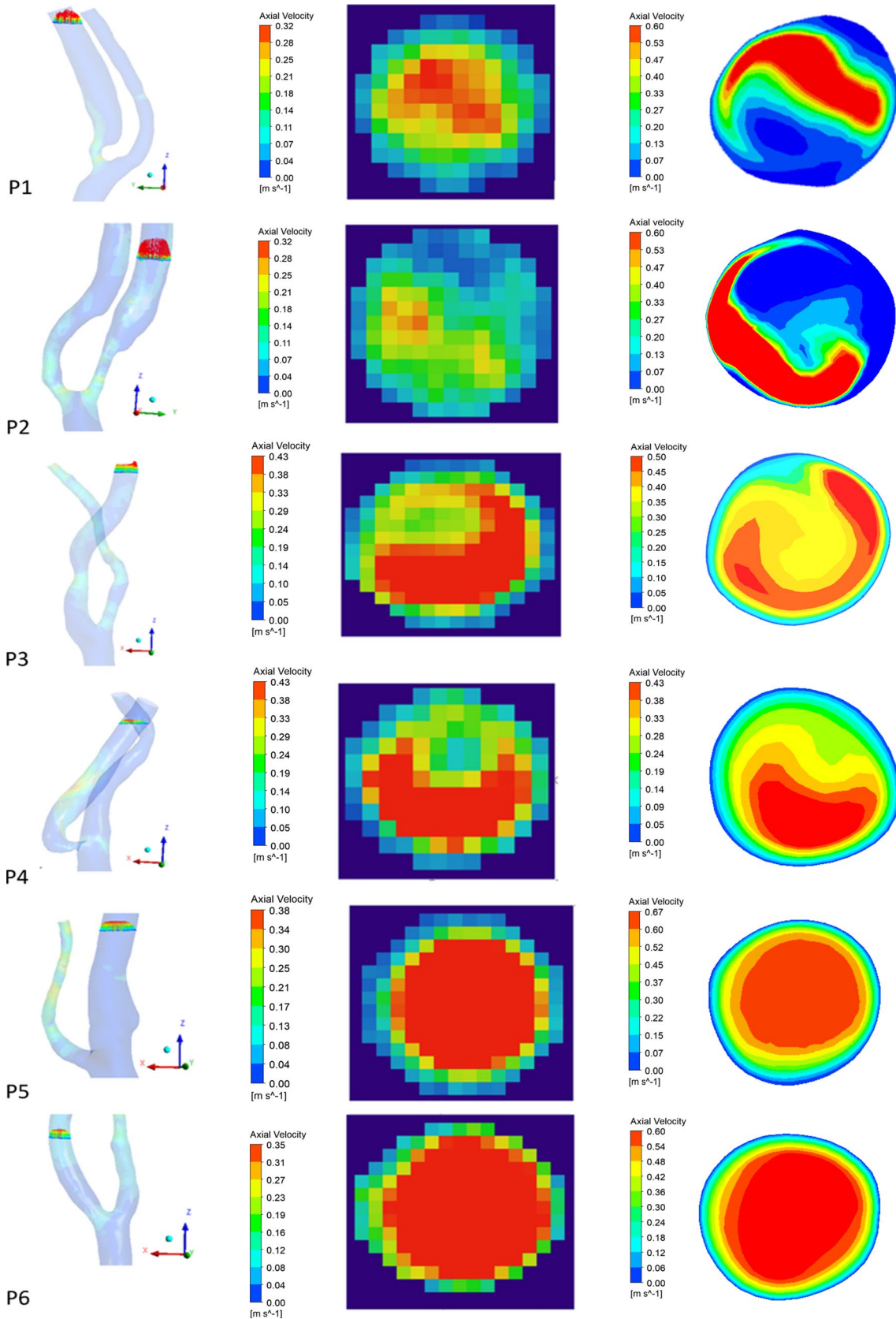
◀Fig. 9 Velocity comparisons between PC-MRI measurements and CFD simulations. Left column: the cross-section location for the comparison and the velocity vectors; mid-column: the axial velocity profiles at systole from PC-MRI measurements. Right column: the axial velocity profiles at systole from CFD simulations

to rheological assumptions on patient-specific geometries and boundary conditions and their effect on WSS descriptors. It can be further developed by including a larger number of patients and considering different haematocrit values.

6 Conclusion

In conclusion, our findings suggest that, for image-based computational simulation of atherosclerotic and healthy carotid arteries, the assumption of a Newtonian model is reasonable for OSI, RRT and pressure gradient, in the context of present geometric and boundary conditions uncertainties. For the maximum and average TAWSS, applying a Newtonian model is also reasonable. For low TAWSS, though, a non-Newtonian model is necessary as the differences between models are higher, especially for the cases with the highest stenosis. The analysis proposed here could provide valuable information with relation to using PC-MRI as a source to define boundary conditions and additionally as a consistency check method. Moreover, as multiple carotid arteries with different degrees of stenosis were evaluated, the results could guide future simulations into the necessity of applying non-Newtonian models to highly stenotic arteries.

References

Ambrosi D, Rozza G, Quarteroni A (2006) Modeling of Physiological Flows. Springer, Berlin

Augst AD, Ariff BMCG, Thom SAG et al (2007) Analysis of complex flow and the relationship between blood pressure, wall shear stress, and intima-media thickness in the human carotid artery. Am J Physiol Circ Physiol 293:H1031–H1037. https://doi.org/10.1152/ajpheart.00989.2006

Berger SA, Jou L (2000) Flows in Stenotic Vessels. Annu Rev Fluid Mech. https://doi.org/10.1146/annurev.fluid.36.050802.122124

Bozzi S, Morbiducci U, Gallo D et al (2017) Uncertainty propagation of phase contrast-MRI derived inlet boundary conditions in computational hemodynamics models of thoracic aorta. Comput Methods Biomech Biomed Engin 20:1104–1112. https://doi.org/10.1080/10255842.2017.1334770

Brust M, Schaefer C, Doerr R et al (2013) Rheology of human blood plasma: viscoelastic versus Newtonian behavior. Phys Rev Lett 110:6–10. https://doi.org/10.1103/PhysRevLett.110.078305

Chen J, Lu XY (2004) Numerical investigation of the non-Newtonian blood flow in a bifurcation model with a non-planar branch. J Biomech 37:1899–1911. https://doi.org/10.1016/j.jbiomech.2004.02.030

Cho YI, Kensey KR (1991) Effects of the non-Newtonian viscosity of blood on flows in a diseased arterial vessel. Part 1: steady flows. Biorheology 28:241–262. https://doi.org/10.3233/BIR-1991-283-415

Cross MM (1965) Rheology of non-Newtonian fluids: a new flow equation for pseudoplastic systems. J Colloid Sci 20:417–437. https://doi.org/10.1016/0095-8522(65)90022-X

DiCarlo AL, Holdsworth DW, Poepping TL (2019) Study of the effect of stenosis severity and non-Newtonian viscosity on multidirectional wall shear stress and flow disturbances in the carotid artery using particle image velocimetry. Med Eng Phys 65:8–23. https://doi.org/10.1016/j.medengphy.2018.12.023

Dong J, Wong KKL, Tu J (2013) Hemodynamics analysis of patient-specific carotid bifurcation : A CFD model of downstream peripheral vascular impedance. 476–491. https://doi.org/10.1002/cnm

Eshtehardi P, Brown AJ, Bhargava A et al (2017) High wall shear stress and high-risk plaque: an emerging concept. Int J Cardiovasc Imaging 33:1089–1099. https://doi.org/10.1007/s10554-016-1055-1

Evju Ø, Valen-Sendstad K, Mardal KA (2013) A study of wall shear stress in 12 aneurysms with respect to different viscosity models and flow conditions. J Biomech 46:2802–2808. https://doi.org/10.1016/j.jbiomech.2013.09.004

Ferguson GG, Eliasziw M, Barr HWK et al (1999) Surgical results in 1415 patients. Stroke 30:1751–1758

Gallo D, Steinman DA, Morbiducci U (2014) An insight into the mechanistic role of the common carotid artery on the hemodynamics at the carotid bifurcation. Ann Biomed Eng 43:68–81. https://doi.org/10.1007/s10439-014-1119-0

Gallo D, Bijari PB, Morbiducci U et al (2018) Segment-specific associations between local haemodynamic and imaging markers of early atherosclerosis at the carotid artery: an in vivo human study. J R Soc Interface. https://doi.org/10.1098/rsif.2018.0352

Gao H, Long Q, Graves M et al (2009) Carotid arterial plaque stress analysis using fluid-structure interactive simulation based on in vivo magnetic resonance images of four patients. J Biomech 42:1416–1423. https://doi.org/10.1016/j.jbiomech.2009.04.010

Gao H, Long Q, Das SK et al (2011) Stress analysis of carotid atheroma in transient ischemic attack patients: evidence for extreme stress-induced plaque rupture. Ann Biomed Eng 39:2203–2212. https://doi.org/10.1007/s10439-011-0314-5

Gharahi H, Zambrano BA, Zhu DC et al (2017) Computational fluid dynamic simulation of human carotid artery bifurcation based on anatomy and volumetric blood flow rate measured with magnetic resonance imaging. Int J Adv Eng Sci Appl Math 8:40–60. https://doi.org/10.1007/s12572-016-0161-6.Computational

Huh HK, Ha H, Lee SJ (2015) Effect of non-Newtonian viscosity on the fluid-dynamic characteristics in stenotic vessels. Exp Fluids 56:1–12. https://doi.org/10.1007/s00348-015-2037-0

Hussain MA, Kar S, Puniyani RR (1999) Relationship between power law coefficients and major blood constituents affecting the whole blood viscosity. J Biosci 24:329–337. https://doi.org/10.1007/BF02941247

Ku DN, Giddens DP, Zarins CK et al (1985) Pulsatile flow and atherosclerosis in the human carotid bifurcation. Ateriosclerosis 5:293–302

LaDisa JF, Olson LE, Molthen RC et al (2005) Alterations in wall shear stress predict sites of neointimal hyperplasia after stent implantation in rabbit iliac arteries. Am J Physiol Circ Physiol 288:H2465–H2475. https://doi.org/10.1152/ajpheart.01107.2004

Lee S-W, Steinman DA (2007) On the relative importance of rheology for image-based CFD models of the carotid bifurcation. J Biomech Eng 129:273. https://doi.org/10.1115/1.2540836

Lee S-W, Antiga L, Steinman DA (2009) Correlations among indicators of disturbed flow at the normal carotid bifurcation. J Biomech Eng 131:061013. https://doi.org/10.1115/1.3127252

Li MX, Beech-Brandt JJ, John LR et al (2007) Numerical analysis of pulsatile blood flow and vessel wall mechanics in different degrees of stenoses. J Biomech 40:3715–3724. https://doi.org/10.1016/j.jbiomech.2007.06.023

Li ZY, Tan FPP, Soloperto G et al (2015) Flow pattern analysis in a highly stenotic patient-specific carotid bifurcation model using a turbulence model. Comput Methods Biomech Biomed Eng 18:1099–1107. https://doi.org/10.1080/10255842.2013.873033

Long Q, Xu XY, Ariff B et al (2000) Reconstruction of blood flow patterns in a human carotid bifurcation: a combined CFD and MRI study. J Magn Reson Imaging 11:299–311. https://doi.org/10.1002/(SICI)1522-2586(200003)11:3%3c299::AID-JMRI9%3e3.0.CO;2-M

Malek AM, Alper SL (1999) Hemodynamic shear stress and its role in atherosclerosis. Stress Int J Biol Stress 282:2035–2042

Mehri R, Mavriplis C, Fenech M (2018) Red blood cell aggregates and their effect on non-Newtonian blood viscosity at low hematocrit in a two-fluid low shear rate microfluidic system. PLoS ONE. https://doi.org/10.1371/journal.pone.0199911

Moradicheghamahi J, Sadeghiseraji J, Jahangiri M (2019) Numerical solution of the Pulsatile, non-Newtonian and turbulent blood flow in a patient specific elastic carotid artery. Int J Mech Sci 150:393–403. https://doi.org/10.1016/j.ijmecsci.2018.10.046

Morbiducci U, Gallo D, Massai D et al (2010) Outflow conditions for image-based hemodynamic models of the carotid bifurcation: implications for indicators of abnormal flow. J Biomech Eng 132:091005. https://doi.org/10.1115/1.4001886

Morbiducci U, Gallo D, Massai D et al (2011) On the importance of blood rheology for bulk flow in hemodynamic models of the carotid bifurcation. J Biomech 44:2427–2438. https://doi.org/10.1016/j.jbiomech.2011.06.028

Morbiducci U, Ponzini R, Gallo D et al (2013) Inflow boundary conditions for image-based computational hemodynamics: impact of idealized versus measured velocity profiles in the human aorta. J Biomech 46:102–109. https://doi.org/10.1016/j.jbiomech.2012.10.012

Osinnski JN, Ku DN, Mukundan S et al (1995) Determination of wall shear stress in the aorta with the use of MR phase velocity mapping. J Magn Reson Imaging 5:640–647. https://doi.org/10.1002/jmri.1880050605

Pirola S, Jarral OA, O'Regan DP et al (2018) Computational study of aortic hemodynamics for patients with an abnormal aortic valve: the importance of secondary flow at the ascending aorta inlet. APL Bioeng 2:026101. https://doi.org/10.1063/1.5011960

Polanczyk A, Podyma M, Stefanczyk L et al (2015) A 3D model of thrombus formation in a stent-graft after implantation in the abdominal aorta. J Biomech 48:425–431. https://doi.org/10.1016/j.jbiomech.2014.12.033

Polanczyk A, Wozniak T, Strzelecki M et al (2016) Evaluating an algorithm for 3D reconstruction of blood vessels for further simulations of hemodynamic in human artery branches. Signal Process Algorithms Archit Arrange Appl Conf Proc SPA. https://doi.org/10.1109/SPA.2016.7763595

Polanczyk A, Podgorski M, Wozniak T, Stefanczyk L (2018) Computational fluid dynamics as an engineering tool for the reconstruction of hemodynamics after carotid artery stenosis operation : a case study. https://doi.org/10.3390/medicina54030042

Polanczyk A, Podgorski M, Polanczyk M et al (2019) A novel method for describing biomechanical properties of the aortic wall based on the three-dimensional fluid-structure interaction model. Interact CardioVasc Thorac Surg 28:306–315. https://doi.org/10.1093/icvts/ivy252

Quemada D (1978) Rheology of concentrated disperse systems III. General features of the proposed non-newtonian model. Comparison with experimental data Rheologic. Rheology 653:643–653

Razavi A, Shirani E, Sadeghi MR (2011) Numerical simulation of blood pulsatile flow in a stenosed carotid artery using different rheological models. J Biomech 44:2021–2030. https://doi.org/10.1016/j.jbiomech.2011.04.023

Robertson AM, Owens RG (2009) Rheology of blood. In: Cardiovascular mathematics. Springer, Berlin, pp 211–242

Schirmer CM, Malek AM (2012) Computational fluid dynamic characterization of carotid bifurcation stenosis in patient-based geometries. Brain Behav. https://doi.org/10.1002/brb3.25

Skiadopoulos A, Neofytou P, Housiadas C (2017) Comparison of blood rheological models in patient specific cardiovascular system simulations. J Hydrodyn 29:293–304. https://doi.org/10.1016/S1001-6058(16)60739-4

Soulis JV, Lampri OP, Fytanidis DK, Giannoglou GD (2011) Relative residence time and oscillatory shear index of non-Newtonian flow models in aorta. In: 10th international workshop on biomedical engineering, pp 0–3. https://doi.org/10.1109/iwbe.2011.6079011

Steinman DA, Thomas JB, Ladak HM et al (2002) Reconstruction of carotid bifurcation hemodynamics and wall thickness using computational fluid dynamics and MRI. Magn Reson Med 47:149–159. https://doi.org/10.1002/mrm.10025

Yang C, Tang D, Yuan C et al (2007) In vivo/ex vivo MRI-based 3D non-newtonian FSI models for human atherosclerotic plaques compared with fluid/wall-only models. C Comput Model Eng Sci 19:233–245. https://doi.org/10.3970/cmes.2007.019.233

Youssefi P, Gomez A, He T et al (2017) Patient-specific computational fluid dynamics—assessment of aortic hemodynamics in a spectrum of aortic valve pathologies. J Thorac Cardiovasc Surg 153:8–20.e3. https://doi.org/10.1016/j.jjtcvs.2016.09.040

Youssefi P, Gomez A, Arthurs C et al (2018) Impact of patient-specific inflow velocity profile on hemodynamics of the thoracic aorta. J Biomech Eng. https://doi.org/10.1115/1.4037857